analytical chemistry

pubs.acs.org/ac Article

Exploring Metabolic Aberrations after Intracerebral Hemorrhage In Vivo with Deuterium Metabolic Spectroscopy Imaging

Xinjie Liu, Qingjia Bao,* Zhuang Liu, Jie Wang, Martins Otikovs, Zhi Zhang, Xin Cheng, Jiazheng Wang, Lucio Frydman, Xin Zhou, Maili Liu, and Chaoyang Liu*

Cite This: *Anal. Chem.* 2024, 96, 15563−15571 Read Online

ACCESS | Metrics & More | Article Recommendations | Supporting Information

ABSTRACT: Aberrations in metabolism after intracerebral hemorrhage (ICH), particularly lactate metabolism, play a crucial role in the pathophysiology and patient outcome. To date, the evaluation of metabolism relies heavily on invasive methods such as microdialysis, restricting a comprehensive understanding of the metabolic mechanisms associated with ICH. This study proposes a noninvasive metabolic imaging method based on ^{2}H magnetic resonance spectroscopy and imaging (^{2}H-MRS/MRSI) to detect metabolic changes after ICH in vivo. To overcome the low-sensitivity limitation of ^{2}H, we designed a new ^{1}H−^{2}H double-resonance coil with ^{2}H-channel active detuning and proposed chemical shift imaging based on the balanced steady-state free precession method (CSI-bSSFP). Compared with the volume coil, the signal-to-noise ratio (SNR) of the new coil was increased by 4.5 times. In addition, the SNR of CSI-bSSFP was 1.5 times higher than that of conventional CSI. These two technologies were applied to measure lactate metabolic flux at different phases of ICH. The results show a higher lactate concentration in ICH rats than in control rats, which is in line with the increased expression of lactate dehydrogenase measured via immunohistochemistry staining (AUC_{Lac_area/Glc_area}: control, 0.08 ± 0.02 vs ICH-3d, 0.39 ± 0.05 vs ICH-7d, 0.18 ± 0.02, $P < 0.01$; H-score: control, 126.4 ± 5.03 vs ICH-3d, 168.4 ± 5.71 vs ICH-7d,133.6 ± 7.70, $P < 0.05$). A higher lactate signal also appeared near the ICH region than in normal brain tissue. In conclusion, ^{2}H-MRS/MRSI shows potential as a useful method for in vivo metabolic imaging and noninvasive assessment of ICH.

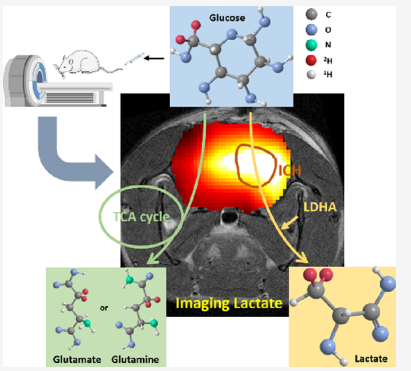

INTRODUCTION

Intracerebral hemorrhage (ICH) is the second most common subtype of stroke, following ischemic stroke, and accounts for about 10−15% of all stroke cases. It is associated with high mortality and long-term disability.[1,2] ICH occurs when cerebral blood vessels rupture, causing a rapid increase in intracranial pressure and hematoma expansion, which leads to secondary brain injury.[3,4] During this process, brain metabolism is disrupted, affecting ionic homeostasis, energy supply, and inflammation.[4−6] Therefore, monitoring metabolic changes is crucial for predicting secondary damage and guiding the subsequent treatment.[7] Currently, the assessment of brain metabolism mainly depends on invasive methods such as microdialysis.[8−10] However, these invasive methods are limited by their inability to provide spatial information about specific metabolic pathways in different regions of the brain.

To date, positron emission tomography (PET) is the most common metabolic detection method that can provide both dynamic and spatial information on brain metabolism.[4,11] PET imaging shows an increase in glucose uptake in the tissues surrounding the hematoma 2−4 days after ICH.[4,12] However, PET only reflects glucose uptake and cannot provide downstream metabolic information after ICH, which could be misleading in the evaluation of cell-specific metabolism in some circumstances.[13] Hyperpolarized ^{13}C magnetic resonance spectroscopy imaging (HP ^{13}C MRSI) has emerged as a diagnostic tool with significant potential for in vivo metabolic imaging.[14,15] Using HP ^{13}C, Guglielmetti et al.[16] showed that the ratio of lactate to pyruvate in the damaged cortex increased as pyruvate dehydrogenase activity decreased at acute (12/24 h) and subacute (7 days) time points after traumatic brain injury. However, HP ^{13}C MRS/MRSI can only effectively observe fast metabolism, such as that of pyruvate with a long T_1 relaxation time.[17]

In this work, we propose a novel noninvasive metabolic imaging method based on ^{2}H-MRS/MRSI to explore metabolic aberrations after ICH. ^{2}H-MRS/MRSI has three main advantages for exploring metabolic aberrations after ICH. First, because of the low natural abundance of ^{2}H nuclei, ^{2}H-MRS/MRSI has almost no background signal without injection of an ^{2}H-labeled substance.[18−20] Second, ^{2}H-labeled metabo-

Received: April 17, 2024
Revised: August 7, 2024
Accepted: September 4, 2024
Published: September 19, 2024

https://doi.org/10.1021/acs.analchem.4c01999
Anal. Chem. 2024, 96, 15563−15571

lites are nonradioactive and minimally affect metabolic pathways, thus enabling the observation of the whole metabolic evolution and metabolic flux rate changes.[18−22] Third, the longitudinal relaxation time T_1 of ^2H is much shorter than that of ^{13}C, allowing for the averaging of many scans within a reasonable acquisition time.[18−20,23] Lastly, the transverse relaxation time of ^2H is long enough to differentiate between chemical shifts of many important metabolites, including glucose and lactate.[19] Therefore, it is possible to obtain high-quality ^2H-MRS/MRSI within a reasonable time for in vivo metabolic studies.

EXPERIMENTAL SECTIONS

Experimental Design. Figure 1A illustrates the entire experimental design. To observe different metabolic phases after ICH, we divided rats into three groups: (1) control group, n = 8; (2) 3 days after ICH (ICH-3d) group, n = 8; and (3) 7 days after ICH (ICH-7d) group, n = 8. We induced ICH in the ICH-3d and ICH-7d groups using stereotactic collagenase injection. To overcome the low sensitivity associated with ^2H detection, we designed a $^1H-^2H$ double-resonance coil with active detuning of the ^2H channel and data acquisition using chemical shift imaging based on the balanced steady-state free precession method (CSI-bSSFP). Then, half of the rats in each group underwent ^2H-MRS with the non-localized spectroscopy sequence that provided high temporal resolution for the whole-brain metabolism, and the other half underwent dynamic chemical shift imaging with the CSI-bSSFP sequence that provided both spatial and temporal information on metabolic aberrations after ICH. Figure 1B shows the MR scan strategy. We quantitatively measured the metabolic flux by analyzing the areas under the curve (AUCs) obtained from the MR experiments in the three groups. After scanning, we collected all animal brains for hematoxylin and eosin (H&E) and immunohistochemical (IHC) staining. Finally, we performed a correlation analysis between the staining indicators and the AUCs to investigate the ability of ^2H-MRS/MRSI to observe lactate metabolic changes caused by concentration changes of the lactate dehydrogenase enzyme at different phases after ICH.

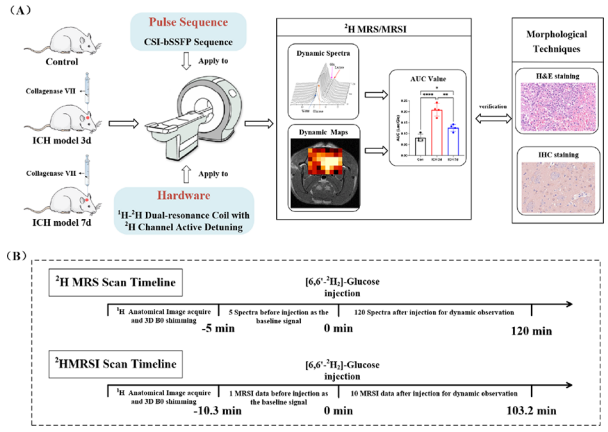

Figure 1. (A) Experimental study design. Three groups of rats [(1) control, (2) 3 days after ICH, and (3) 7 days after ICH] were imaged using ^2H-MRS/MRSI. Here, two optimized technologies ($^1H-^2H$ double-resonance coil with ^2H channel active detuning and CSI-bSSFP pulse sequence) are introduced to increase the SNR for ^2H-MRS/MRSI. After the scanning, all the animal brains are collected for morphological analysis (H&E and IHC staining). The results of quantitative analysis (AUC) from dynamic spectra and maps are validated by staining results of ICH. (B) MR scan timeline. Before the MRS and MRSI scanning, ^1H anatomical image and 3D B_0 shimming are performed. Then, baseline data are acquired (MRS: five scans, 5 min; MRSI: one scan, 10 min). [6,6′-$^2H_2$]-Glucose (2 g/kg body weight, 1 mL) is injected for dynamic MRS/MRSI scanning (MRS: 120 min; MRSI 103.2 min).

Animal Protocol. All animal procedures were approved by the Animal Care and Use Committee of the Innovation Academy for Precision Measurement Science and Technology, Chinese Academy of Sciences (APM22022A), and were conducted according to the National Institutes of Health animal care guidelines. Adult male Sprague−Dawley rats (n = 24, 7−8 weeks old, and 250−280 g) were obtained from the Hunan Slac JingDa Laboratory Animal Company (Hunan, China). They were adaptively fed in a 12/12 h light−dark cycle in a temperature- and moisture-autocontrolled specific pathogen-free animal room.

We used the traditional intracerebral collagenase injection method to establish the ICH animal model.[24] Collagenase VII (Sigma-Aldrich, St. Louis, MO) was dissolved in physiological saline at 0.2 U/μL. The ICH model construction was induced in a stereotactic injection system, and collagenase VII saline solution (2 μL) was intracerebrally injected into the animal's caudate putamen nucleus (CPU) in 5 min. The detailed steps for ICH animal model generation are described in Section 3 of the Supporting Information.

After MRI/MRSI, all brains of the animals were collected and fixed in a 4% paraformaldehyde solution. The fixed brains were then embedded in paraffin and cut into sections (4 μm) for staining, as described in Section 3 of the Supporting Information. The sections were stained with H&E solution after paraffin removal. For IHC, a primary antibody (Proteintech, Rosemont, IL) was used to detect lactate dehydrogenase A (LDHA). H&E and IHC images were obtained using an Olympus FSX100 microscope (Olympus, Tokyo, Japan) and scanned using a Pannoramic MIDI (3DHISTECH, Budapest, Hungary). H&E and IHC analyses were conducted using the Image-Pro Plus software (version 6.0, Media Cybernetics, Rockville, MD; U12388-02, HAMAMATSU, Hamamatsu, Japan).

Phantom Experiment. All MRI data were acquired with the Bruker BioSpec 7.0 T/20 cm MRI scanner (Paravision 5.1; Bruker, Billerica, MA). Given that the in vivo experiments could not accurately reflect the SNR improvement owing to the constantly changing concentration of metabolites in rats, two phantoms were prepared to test the coil and pulse sequences. The first phantom was made of 50% ^1H_2O water and 50% ^2H_2O water (99.96 atom % ^2H; Aladdin Scientific, Riverside, CA) to evaluate the SNR of the three coils. For ^2H images, a FLASH sequence with the following parameters was used for the SNR comparison: TR/TE = 100/4 ms, flip angle = 30°, FOV = 50 × 50 mm^2, matrix = 96 × 96, bandwidth = 50 kHz, slice thickness = 2 mm, number of repetitions = 2, and number of averages = 2. We also compared the ^1H coil with the FLASH images and performed acquisition with refocused resonance (RARE) images. The parameters and results are described in Section 1 of the Supporting Information. The second phantom was composed of two chemical compounds to compare the CSI sequences. One was ^2H-glucose at 20 mM, and the other was ^2H-lactate at 15 mM. The conventional 2D CSI and CSI-bSSFP pulse sequence parameters were as follows: FOV = 30 × 30 mm^2, slice thickness = 10 mm, TR =

https://doi.org/10.1021/acs.analchem.4c01999
Anal. Chem. 2024, 96, 15563−15571

20 ms, matrix = 11 × 11, 80 points in the spectral dimension, bandwidth = 4596 Hz, 256 averages, and total time of 10.32 min.

In Vivo Experiment. During the in vivo MRI experiment, all rats were anesthetized with isoflurane mixed with oxygen (3% for induction, 1.5−2% for maintenance), and the respiratory rate (30−50 times/min) was continuously monitored during the scan. The body temperature was stabilized at 37 °C with water circulation. The MR scan timeline is shown in Figure 1B. ^{1}H anatomical T_2-weighted proton images were acquired using the RARE sequence with the following parameters: TR/TE = 2500/24 ms, field of view = 30 × 30 mm^2, matrix = 256 × 256, slice thickness = 1 mm, RARE factor = 8, and number of averages = 8. The acquisition of anatomical MR images was followed by 3D B_0 shimming (second-order SH sheeting), which resulted in approximately 40−60 Hz across a 7 × 5 × 10 mm volume. [6,6′-$^{2}H_2$]-Glucose (Sigma-Aldrich) was manually injected into the rats through a tail vein catheter at a rate of approximately 0.1 mL/s after the acquisition. For ^{2}H-MRS, non-localized spectroscopy was used for data acquisition over 120 min with the following parameters: TR = 70.59 ms, flip angle = 20°, number of averages = 420, points = 256, and bandwidth = 4 kHz. In addition, we saturated the signals outside of the rat brain by introducing a saturation slice. For MRSI, the 2D CSI-bSSFP sequence was acquired using a flip angle of 60° with phase-encoding gradients encoding an 11 × 11 k-space matrix with an FOV of 30 × 30 mm^2 and a slice thickness of 10 mm. Data were acquired at 80 complex points with a sweep width of 4596 Hz and TR of 20 ms, and each image took 10.32 min to acquire with 256 averages. The carrier frequency was placed in the middle of these sites' chemical shifts (2.5 ppm).

^{2}H-MRS/MRSI Data Analysis. The NMR spectra were zero-filled and fitted using the AMARES toolbox[25] in MATLAB (R2014a, MathWorks, Natick, MA). Prior knowledge of the relative chemical shifts and line widths was used to restrict the fitting function. The fitted water and metabolite peaks were converted to concentration based on the natural abundance ^{2}H-labeled water concentration of 12.60 mM and T_1/T_2 values.[18,21] The detailed theories and calculation formulas can be found in Section 4 of the Supporting Information. The data for the chemical shift images were obtained by using zero-filling, matched-weighting filters in both the temporal and spectral domains (3 Hz apodization) and 3D FT.

Statistical Analysis. Statistical and graphical analyses were performed. Data were presented as mean ± standard deviation (SD). Ordinary one-way ANOVA analysis was performed for comparisons among multiple groups. Pearson's correlation coefficient was derived to analyze the correlation between imaging and pathology. Statistical significance was set at $P < 0.05$ after multiple comparison correction.

RESULTS AND DISCUSSION

^{1}H−^{2}H Double-Resonance Coil with Active Detuning of the ^{2}H Channel. We designed and implemented a novel ^{1}H−^{2}H double-resonance coil to simplify the coregistration of anatomy and metabolic images, as shown in Figure 2. To achieve higher SNR and B_1^+ field homogeneity for ^{2}H metabolism imaging, we used the active detuning saddle volume design for the ^{2}H excitation coil and the double-loop surface design for the ^{2}H reception coil. We actively detuned the surface coil when the saddle coil is in transmission mode to excite the spins and vice versa. As shown in Figure 2A, in the order from outside to inside, the coil parts are the shielding layer, ^{1}H transceiver birdcage coil (length 70 mm, diameter 72 mm), ^{2}H transmit saddle coil (length 60 mm, diameter 48 mm), and ^{2}H receiver double-loop surface coil (length 18 mm, width 18 mm). To reduce the shielding effect of the ^{1}H birdcage coil, we adopted a saddle design with an open angle for the ^{2}H transmit coil, which allowed the radiofrequency (RF) field of the ^{1}H birdcage coil to pass through, as demonstrated in the Supporting Information (Figure S3). We adopted a double-loop structure for the ^{2}H surface receiver coil to increase the inductance and thus improve the Q value and SNR for ^{2}H-MRS/MRSI. To avoid strong coupling between the ^{2}H saddle and surface coils, the two coils had an active detuning design to ensure that they were operated in time-sharing mode, which was controlled by the tuning/detuning switch and the BLANK unit of the transceiver system, as shown in Figure 2A. Moreover, we used the protection circuit for the ^{2}H surface coil to prevent the high-power RF signal emitted by the saddle coil during the transmission phase and to protect the preamplifier. Section 1 of the Supporting Information shows the detailed design of the coils.

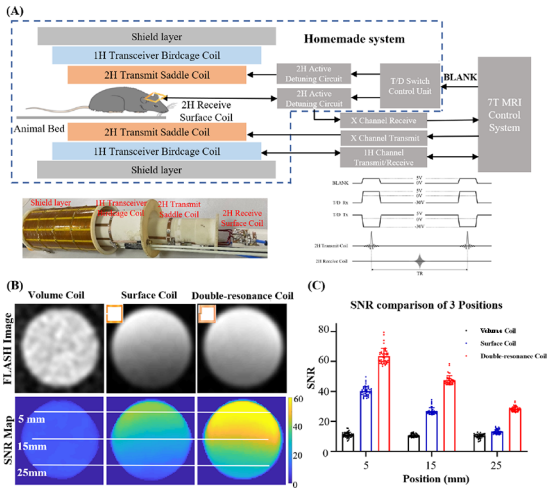

Figure 2. Fabrication and performance of the ^{1}H−^{2}H double-resonance coil with ^{2}H channel active detuning. (A) The coil consists of four parts: a shielding layer, a ^{1}H transceiver birdcage coil, a ^{2}H transmit saddle coil, and a ^{2}H receiver double-loop surface coil. The coil is connected to the supporting hardware facilities for active detuning. (B) The ^{2}H images based on FLASH and the calculated SNR map were obtained with different coils: the volume coil, the single-loop surface coil, and the double-resonance coil. The SNRs are calculated from the FLASH images. (C) The SNR values at three depths (5, 15, and 25 mm) along the white line in panel B. The double-resonance coil achieves a 4.5- and a 1.7-fold improvement in SNR at the 15 mm depth compared to the volume and surface coils, respectively.

To demonstrate the improved SNR with the double-resonance coil, we also implemented two traditional preclinical coils for comparison: a transceiver saddle volume coil (length 60 mm, diameter 48 mm) and a transceiver surface coil (length 18 mm, width 18 mm). Before scanning, each coil was finely tuned after being positioned in the MR bore with tuning rods. The axial fast low-angle shot (FLASH) ^{2}H-MRI images and calculated SNR maps for the phantom with different coils are presented in Figure 2B. From the SNR comparison in Figure 2C, it can be seen that the double-resonance coil can increase the SNR by 5.7 (5 mm in depth), 4.5 (15 mm in depth), and

https://doi.org/10.1021/acs.analchem.4c01999
Anal. Chem. 2024, 96, 15563−15571

2.1 (25 mm in depth) times compared to the saddle volume coil. Compared to the single-loop surface coil, the double-resonance coil is able to achieve a 1.5-fold (5 mm depth), 1.7-fold (15 mm depth), and 2.7-fold (25 mm depth) increase in SNR. As the depth increases, the SNR gains are enhanced because the B_1 excitation field of the saddle excitation coil has greater homogeneity than that of the surface coil. Thus, the results indicated that the double-resonance coil can acquire higher SNR images than both the volume coil and the single-loop surface coil.

CSI-bSSFP Sequence. In addition to coils, the pulse sequence also plays a crucial role for improving the SNR. The bSSFP method is a well-known technology that provides high SNR and short imaging times.[23,26−28] In a previous study, Peters et al.[23] applied a multiecho (ME) bSSFP to ^{2}H-MRSI acquisition, which achieved a three- to fivefold increase in SNR compared to conventional CSI. The calculation of the ^{2}H images for different chemical species is based on the phase evolution and assumed frequency with chemical shift, similar to the Dixon method. However, ME-bSSFP has some drawbacks, such as increased echo time (TE) and repetition time (TR) and B_0 inhomogeneity artifacts, which can affect the accuracy of the ^{2}H images. Thus, in some situations, the ^{2}H images are not accurate.[23] Herein, we developed the CSI-bSSFP sequence to reduce the TE/TR of ME-bSSFP and to increase SNR, as shown in Figure 3A. Compared with

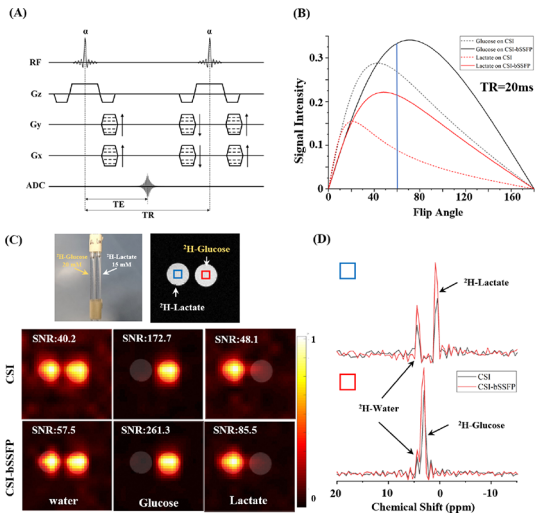

Figure 3. CSI-bSSFP sequence and its performance. (A) The CSI-bSSFP sequence refocuses all gradients during one repetition scan. (B) The simulated signal intensity changes with the flip angle for glucose and lactate with conventional CSI and CSI-bSSFP sequences. (C) The ^{2}H-MRSI images of different chemical shifts overlapped with the ^{1}H T_2-weighted images and the corresponding SNR values. CSI-bSSFP improves the SNR of ^{2}H-water by 1.4 times, ^{2}H-glucose by 1.5 times, and ^{2}H-lactate by 1.8 times compared to CSI. (D) The ^{2}H spectra of the same voxel position in the phantom are indicated by the blue and red squares in panel C.

conventional CSI, all gradients were refocused during the repetition time. The details of the CSI-bSSFP sequence are described in Section 2 of the Supporting Information. To obtain a higher SNR, we also tried to optimize the flip angle for CSI-bSSFP with the following parameters:[18] TR, 20 ms; T_1/T_2 of glucose, 64/32 ms; and T_1/T_2 of lactate, 297/61 ms. Figure 3B shows how the signal intensity changes with the flip angle. The optimal flip angles of glucose and lactate were 72 and 50°, respectively. We chose 60° as the flip angle considering the low concentration and importance of lactate.

To evaluate the SNR increment of CSI-bSSFP, a phantom containing three chemical compounds (^{2}H-water: ∼10 mM, ^{2}H-glucose: ∼20 mM, ^{2}H-lactate: ∼15 mM) was used to compare the SNRs. Figure 3C shows the ^{2}H-MRSI images of different chemical shifts overlapped with the ^{1}H T_2-weighted images and the corresponding SNR values. The CSI-bSSFP sequence improved the SNR of ^{2}H-water by 1.4 times (40.2 vs 57.5), that of ^{2}H-glucose by 1.5 times (172.7 vs 263.1), and that of ^{2}H-lactate by 1.8 times (48.1 vs 85.5) compared to the conventional CSI sequence. Figure 3D shows the voxel spectrum from CSI and CSI-bSSFP, demonstrating that the SNRs of the metabolites were enhanced with the CSI-bSSFP sequence.

Dynamic In Vivo ^{2}H Metabolic Spectra for Different Phases of ICH. We injected [6,6′-$^2H_2$]-glucose into the rats' tail vein and measured the ^{2}H dynamic spectra in vivo for 2 h using the non-localized spectroscopy sequence (Figure 4A−

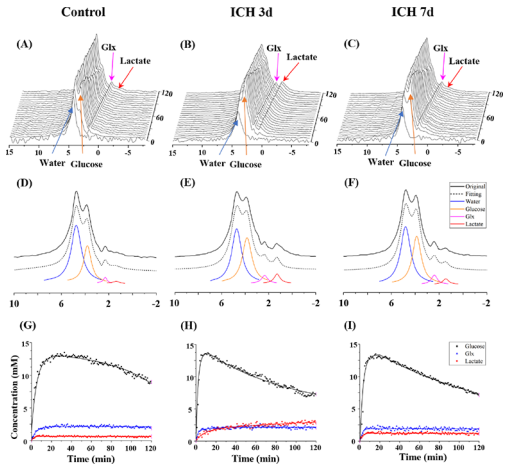

Figure 4. Dynamic ^{2}H spectra of in vivo glucose metabolism after [6,6′-$^2H_2$]-glucose injection. Panels A, B, and C show the ^{2}H spectra of control, ICH-3d, and ICH-7d rats, respectively. We recorded all the spectra within 120 min of injecting [6,6′-$^2H_2$]-glucose (2 g/kg weight). Panels D−F show the fitting results of the sum of all the dynamic spectra with AMARES.[25] Panels G−I show the metabolic dynamic curves of glucose, glutamate/glutamine (Glx), and lactate. Original, the spectrum obtained from direct Fourier transform; Fitting, the summed fitting spectrum of all compounds; Water, Glucose, Glx, and Lactate, indicated the fitting spectrum of the compounds, respectively.

C). Figure 4D−F compares the sum of all the dynamic spectra and their fitting results with AMARES for the three groups: control, ICH at day 3 (ICH-3d), and ICH at day 7 (ICH-7d). The lactate level was significantly higher in ICH-3d than in the control group. Figure 4G−I shows the metabolic dynamic curves for glucose, glutamate/glutamine (Glx), and lactate after injecting [6,6′-$^2H_2$]-glucose. The curves are calculated by fitting every spectrum with AMARES[25] to obtain the metabolic concentrations. The concentration of [6,6′-$^2H_2$]-glucose reached its peak at around 15 min in all three groups and then decreased as the brain consumed glucose. However, the control and ICH-3d rats had significantly different glucose metabolisms with the slowest and fastest glucose declines, respectively. Moreover, the ICH-3d rats had the lowest remaining glucose concentration after 120 min (control, 7.04

https://doi.org/10.1021/acs.analchem.4c01999
Anal. Chem. 2024, 96, 15563−15571

mM vs ICH-3d, 4.62 mM vs ICH-7d, 5.73 mM). The difference in metabolism was more evident in lactate, which was lower than that of Glx in both the control and ICH-7d groups. In contrast, the ICH-3d rats had higher lactate than Glx, indicating a much higher lactate production.

Glutamate and glutamine (Glx) are typically considered the products of oxidative metabolism, whereas lactate is the product of anaerobic respiration.[18] Therefore, we calculated the dynamic concentration ratios of lactate to glucose (Lac/Glc) and Glx (Lac/Glx) to measure the rate of anaerobic metabolism and the proportion relative to aerobic metabolism and displayed them in Figure 5A,C. Each point in the figure represents the ratio value at a specific time point for one rat, and the shaded area shows the data range of all rats in the group. The results indicated that the ICH-3d group had significantly higher Lac/Glc and Lac/Glx ratios than the control group. The ICH-7d group had a lower Lac/Glx ratio than the ICH-3d group, but it is still higher than that in the control group. We also computed the areas under the curve (AUCs) of Lac/Glc and Lac/Glx for the three groups and displayed them in Figure 5B,D. The ICH-3d group had significantly higher AUCs of Lac/Glc and Lac/Glx than the ICH-7d and control groups ($AUC_{Lac/Glc}$: control, 0.08 ± 0.02 vs ICH-3d, 0.21 ± 0.03 vs ICH-7d, 0.13 ± 0.02, $P < 0.05$; $AUC_{Lac/Glx}$: control, 0.40 ± 0.09 vs ICH-3d, 0.94 ± 0.11 vs ICH-7d, 0.55 ± 0.12, $P < 0.05$). Figures 4 and 5 show that the ICH-3d rats have lactate levels much higher than those of the ICH-7d and control rats, indicating more anaerobic metabolism. This is due to ICH disrupting cerebral blood flow and oxygen delivery, leading to tissue hypoxia and ischemia. Consequently, brain cells switch to anaerobic glycolysis, which increases lactate production.[29,30]

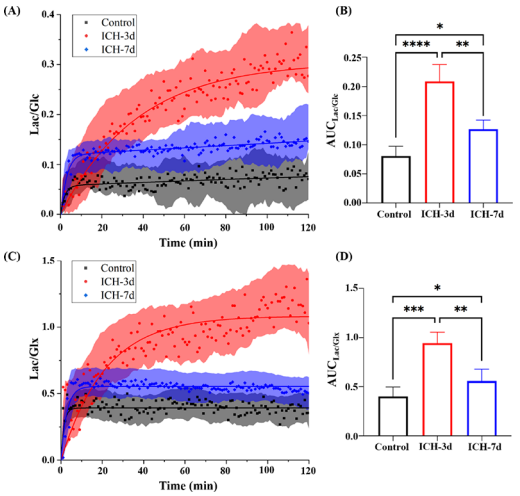

Figure 5. Dynamic concentration ratios of lactate to glucose (Lac/Glc) (A) and to Glx (Lac/Glx) (C) after [6,6′-$^2H_2$]-glucose injection. The lines represent the best fit of the kinetic model. We calculated the areas under the curve (AUCs) of lactate to glucose (Lac/Glc) and to Glx (Lac/Glx) (B and D). Each point in the figure shows the ratio value at a specific time point for one animal, and the shaded area shows the data range of all animals in the group (*$p < 0.05$, **$p <$ 0.01, and ***$p < 0.001$ by one-way ANOVA with Tukey's multiple comparison test).

Localization of Lactate by Dynamic In Vivo ^2H Metabolic Images. We also obtained ^2H-MRSI maps of the metabolites (water, glucose, Glx, and lactate) using the CSI-bSSFP sequence after injecting [6,6′-$^2H_2$]-glucose. We acquired 10 dynamic ^2H-MRSI metabolism maps over a total of 103.2 min. We overlaid one of these metabolic images during 20.6−30.9 min on the corresponding ^1H T_2-weighted anatomical image (Figure 6A). The ^2H-MRSI maps showed higher lactate levels in the ICH area than in the normal brain for both the ICH-3d and ICH-7d groups. We also plotted the dynamic curves of glucose and lactate levels in the ICH area (red box in Figure 6A) and normal brain tissue (blue box in Figure 6A) of the control, ICH-3d, and ICH-7d rats, as shown in Figure 6B. We clearly observed a significant rise in the lactate level in the ICH area (from 0 to 3.29 mM) in the ICH-3d group, whereas the lactate level in the normal brain tissue stayed almost the same. In the ICH-7d group, we also noted an increase in lactate in the ICH area, but it was less than that in the ICH-3d group. For all three groups, the glucose level in the ICH area and normal brain tissue reached a peak at approximately 10 min, after which its level began to drop.

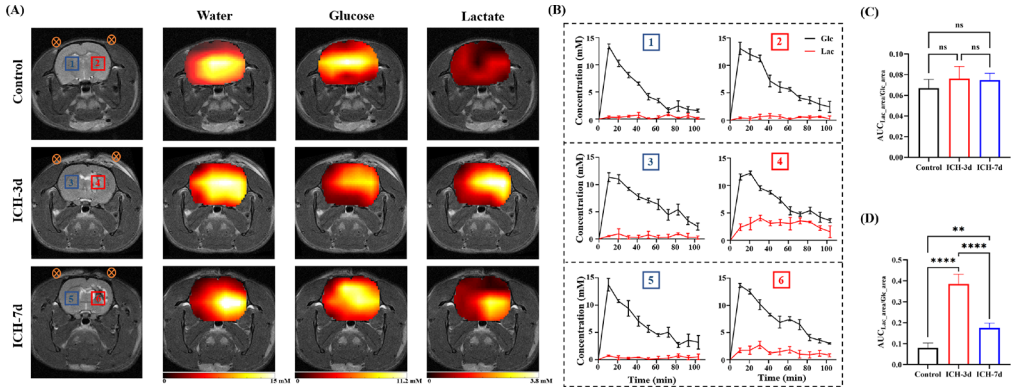

Figure 6. ^2H-MRSI of deuterated water, glucose, and lactate concentrations in control, ICH-3d, and ICH-7d rats. (A) ^1H axial anatomical image was acquired using the rapid acquisition with refocused echo (RARE) sequence. The orange symbol represents the position of the ^2H surface receive coil. Metabolite maps were calculated from the CSI-bSSFP sequence acquired at the specified time (20.6−30.9 min) after [6,6′-$^2H_2$]-glucose injection. The color coding represents millimolar concentrations derived from the peak amplitudes of the initial ^2H water. We plotted the dynamic curves of glucose/lactate concentrations in and out the ICH area for three rat groups (B) and analyzed the AUCs. (C) Comparison of AUCs of Lac/Glc in the normal brain tissue area for all the three group rodents. (D) Comparison of AUCs of Lac/Glc in the ICH area for all the three group rodents (ns: not significant, **$p < 0.01$, and ****$p < 0.0001$ by one-way ANOVA with Tukey's multiple comparison test).

https://doi.org/10.1021/acs.analchem.4c01999
Anal. Chem. 2024, 96, 15563−15571

To compare lactate production rates between the ICH area and normal tissue in different phases after ICH, we also compared the AUCs of Lac/Glc in the ICH and normal brain tissue areas (AUC_{Lac_area/Glc_area}) for all three groups, shown in Figure 6C. In normal brain tissue, the AUCs remained consistently low across all three groups, with no significant difference observed (control, 0.07 ± 0.01 vs ICH-3d, 0.08 ± 0.01 vs ICH-7d, 0.07 ± 0.01; $P > 0.05$) (Figure 6C). The AUCs of the ICH area of the ICH-3d group were significantly higher than those of the ICH-7d and control groups (control, 0.08 ± 0.02 vs ICH-3d, 0.39 ± 0.05 vs ICH-7d, 0.18 ± 0.02; $P < 0.01$) (Figure 6D). The lactate map during 20.6 and 30.9 min is presented as a color map (Figure 7B), and an interpolated color-coded map is also shown (Figure 7C). In Figure 7D, we presented the ^{2}H spectra from the voxels at different distances of the ICH area.

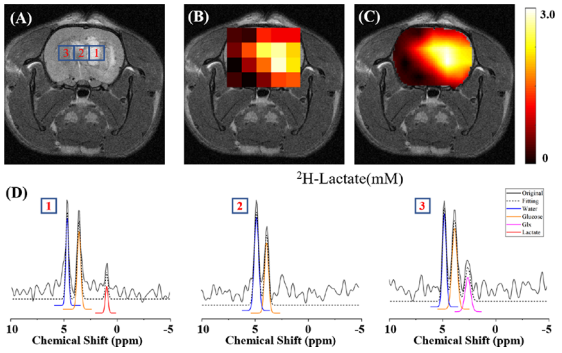

Figure 7. ^{2}H-MRSI comparison of different localized spectra of in vivo for ICH-3d rats after [6,6′-$^2H_2$]-glucose injection. (A) ^{1}H axial slice image showing the ICH lesion and individual voxel positions selected from the ^{2}H-MRSI grid. (B) A color-coded ^{2}H-lactate MRSI grid is overlaid on the anatomical image. (C) Interpolated color-coded map based on data shown in panel B. (D) The ^{2}H spectra and the fitting results from the different voxels are indicated in panel A. Original, the spectrum obtained from direct Fourier transform; Fitting, the summed fitting spectrum of all compounds; Water, Glucose, Glx, and Lactate, indicated the fitting spectrum of the compounds, respectively. The fitting spectrum is not displayed when the signal strength is lower than the noise.

Figures 4 and 6 illustrate the metabolic aberrations after ICH using ^{2}H-MRS/MRSI. Both methods measure lactate production, and metabolic flux is calculated as the dynamic ratio of lactate to glucose (Lac/Glc). Compared to ^{2}H-MRS with non-localized spectroscopy sequence, ^{2}H-MRSI obtained with CSI-bSSFP can provide not only dynamic metabolic information that indicates the metabolic flux but also spatial information on metabolic abnormalities in the ICH area. Although the temporal resolution of ^{2}H-MRSI (~10 min) is much lower than that of ^{2}H-MRS (~1 min), it can provide spatial information that can distinguish the normal brain tissue and ICH areas. In our previous study,[31] we tried to measure the metabolic aberrations after ICH with in vivo ^{1}H-MRS, and the results showed that lactate accumulation can be observed with in vivo ^{1}H-MRS. However, ^{1}H-MRS is limited to observing steady-state metabolic processes and cannot capture dynamic metabolic processes, such as the conversion of glucose to lactate. Additionally, the quantitative measurement of ^{1}H-MRS spectra is often challenging because of the influence of complex interference signals, including lipid signals and inhomogeneous magnetic fields after hemorrhage.[32]

Therefore, ^{2}H-MRS/MRSI is a promising noninvasive technique for studying energy metabolism in vivo.[18−23,33−35] Compared to the popular clinical metabolic imaging method PET, it has the advantage of nonradiation properties and biochemical safety (minimal impact on metabolic processes).[18−22] Compared to the HP ^{13}C method, ^{2}H-MRS/MRSI is more accessible in the clinical setting and can be used to observe slow metabolism (>2 h).[18−20,23] Because deuterated tracers can be enzymatically processed and incorporated into various metabolic intermediates and products, ^{2}H-MRS/MRSI can be used to follow the various compounds in vivo by measuring signal changes.[18−23,33−35]

Pathological Changes in Brain Tissue. To verify the results of ^{2}H-MRS/MRSI in vivo experiments, all brains of the animals were collected for H&E and IHC staining after completing the MRI/MRSI scanning. Figure 8 illustrates the

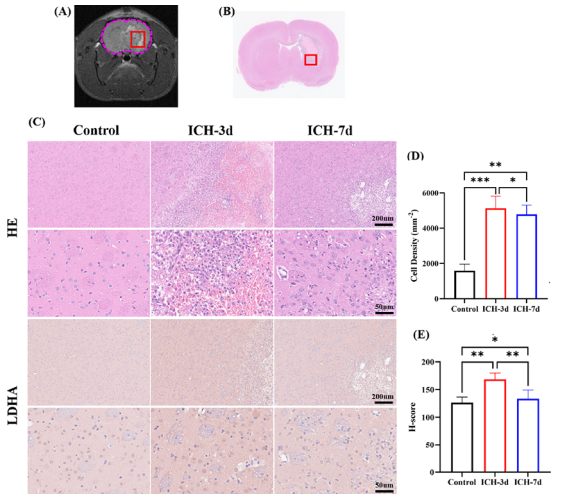

Figure 8. Results of H&E and IHC staining for the three groups. After the MR scan (A), the brain slices (B) of ICH rats are stained with H&E and IHC reagents at different phases of ICH. The first and second rows in panel C are the results of H&E staining (200 and 50 μm) for the ICH area (red box in B), and the third and fourth rows are the results of IHC staining for LDHA (200 and 50 μm). The cell density (D) and H-scores (E) for the three rat groups are also analyzed (*$p < 0.05$, **$p < 0.01$, and ****$p < 0.0001$ by one-way ANOVA with Tukey's multiple comparison test)

results of the biochemical slice staining. Figure 8A,B represents the magnetic resonance T_2-weighted image and the corresponding brain slice in close proximity. However, because of the difference in resolution between the slices (4 μm thickness) and MRI (2 mm thickness), the MRI and biochemical staining do not represent the exact same slice location. The two top rows of Figure 8C show the H&E staining results of ICH areas at different resolutions (200 and 50 μm), which reveal noticeable abnormalities 3 days after ICH induction, including extensive cell proliferation and a significant accumulation of red blood cells. After 7 days, the number of red blood cells decreased. The two bottom rows of Figure 8C show the result of IHC staining for LDHA, an essential enzyme for lactate metabolism, at different resolutions (200 and 50 μm). The result demonstrates a significantly higher expression of LDHA in the ICH area in the ICH-3d group than that in the control group. This observation

https://doi.org/10.1021/acs.analchem.4c01999
Anal. Chem. 2024, 96, 15563−15571

substantiates our ^{2}H-MRS/MRSI measurements that indicated an elevated lactate concentration. The analysis of the cell density for H&E and H-score for LDHA expression in ICH area (Figure 8D,E) also showed significantly higher values in the ICH-3d group than in the control and ICH-7d groups (cell density: control, 1593 ± 184.1 vs ICH-3d, 5123 ± 344.2 vs ICH-7d, 4783 ± 265.9, $P < 0.05$; H-score: control, 126.4 ± 5.03 vs ICH-3d, 168.4 ± 5.71 vs ICH-7d,133.6 ± 7.70, $P < 0.05$).

Quantitative analysis of ^{2}H-MRS/MRSI and IHC results showed significant differences in AUCs, cell density, and H-scores among the three groups. To investigate whether ^{2}H-MRS/MRSI reflected pathological changes in ICH, correlation analysis was performed among AUCs ($AUC_{Lac/Glc}$, $AUC_{Lac/Glx}$, and AUC_{Lac_area/Glc_area}), cell density, and H-score (Figure 9).

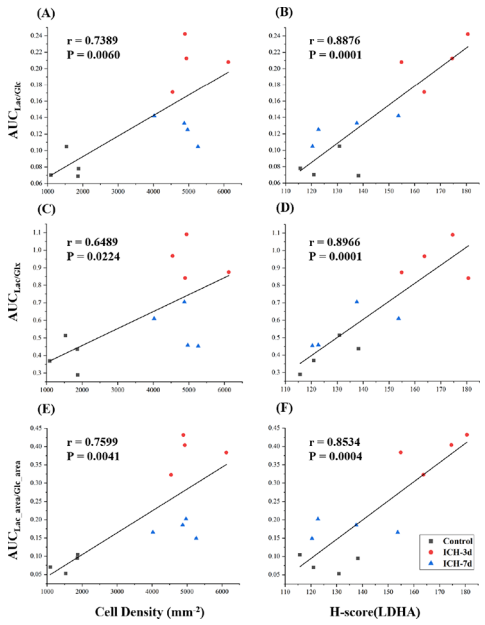

Figure 9. Correlation analysis between the AUCs ($AUC_{Lac/Glc}$, $AUC_{Lac/Glx}$, AUC_{Lac_area/Glc_area}), cell density (A, C, E), and H-scores for LDHA expression (B, D, and F). The AUCs had a strong positive correlation with cell density ($AUC_{Lac/Glc}$: $r = 0.739$, $P = 0.006$; $AUC_{Lac/Glx}$: $r = 0.649$, $P = 0.022$; AUC_{Lac_area/Glc_area}: $r = 0.759$, $P = 0.004$) and H-scores ($AUC_{Lac/Glc}$: $r = 0.888$, $P = 0.0001$; $AUC_{Lac/Glx}$: $r = 0.897$, $P = 0.0001$; AUC_{Lac_area/Glc_area}: $r = 0.853$, $P = 0.0004$).

Specifically, a correlation analysis was performed between the AUC of ^{2}H-MRS from whole brain ($AUC_{Lac/Glc}$ and $AUC_{Lac/Glx}$), cell density, and H-score, as shown in Figure 9A–D. Furthermore, to investigate the metabolic changes in the specific ICH area, we also performed correlation analysis between the AUC of ^{2}H-MRSI from ICH area voxels (AUC_{Lac_area/Glc_area}), cell density, and H-score, as shown in Figure 9D,E. The results showed that the AUCs were strongly positively correlated with cell density ($AUC_{Lac/Glc}$: $r = 0.739$, $P < 0.006$; $AUC_{Lac/Glx}$: $r = 0.649$, $P < 0.022$; AUC_{Lac_area/Glc_area}: $r = 0.759$, $P < 0.004$) and H-score ($AUC_{Lac/Glc}$: $r = 0.888$, $P < 0.0001$; $AUC_{Lac/Glx}$: $r = 0.897$, $P < 0.0001$; AUC_{Lac_area/Glc_area}: $r = 0.853$, $P < 0.0004$). This indicated that the occurrence of ICH could increase cell density and LDHA expression, resulting in high lactate concentration.

CONCLUSIONS

In this work, we provide a noninvasive metabolic imaging solution based on optimized ^{2}H-MRS/MRSI to measure lactate metabolic flux in different phases of ICH. To overcome the low-sensitivity problem of ^{2}H, we designed and implemented a ^{1}H–^{2}H double-resonance coil with active detuning of ^{2}H channel and used CSI-bSSFP for imaging data acquisition. With these new technologies, dynamic MRS and MRSI were used to measure lactate changes at different phases (3 and 7 days) after ICH. Quantitative analysis of the AUCs for ^{2}H-MRS/MRSI shows that the lactate concentration in ICH rats was higher than that in control rats, in line with the expression of LDHA as measured via IHC. A higher lactate signal also appeared near the ICH area compared to the normal brain tissue. Together, these results demonstrate that the optimized ^{2}H-MRS/MRSI has great potential for the in vivo noninvasive diagnosis of ICH.

ASSOCIATED CONTENT

Supporting Information

The Supporting Information is available free of charge at https://pubs.acs.org/doi/10.1021/acs.analchem.4c01999.

Detailed information for ^{1}H–^{2}H double-resonance coil with ^{2}H channel active detuning; optimization of the CSI-bSSFP sequence; surgery and immunohistochemical analysis on rats; ^{2}H/HOD natural abundance and metabolite concentration conversion theory; and the metabolic dynamic changes for glucose, Glx, and lactate (PDF)

AUTHOR INFORMATION

Corresponding Authors

Qingjia Bao − *State Key Laboratory of Magnetic Resonance and Atomic and Molecular Physics, Innovation Academy for Precision Measurement Science and Technology, Chinese Academy of Sciences, Wuhan 430071, China; University of Chinese Academy of Sciences, Beijing 100864, China*; Phone: (+86) 18164106809; Email: qingjia.bao@apm.ac.cn

Chaoyang Liu − *State Key Laboratory of Magnetic Resonance and Atomic and Molecular Physics, Innovation Academy for Precision Measurement Science and Technology, Chinese Academy of Sciences, Wuhan 430071, China; University of Chinese Academy of Sciences, Beijing 100864, China; Optics Valley Laboratory, Hubei 430074, China*; Phone: (+86) 13971309497; Email: chyliu@apm.ac.cn

Authors

Xinjie Liu − *State Key Laboratory of Magnetic Resonance and Atomic and Molecular Physics, Innovation Academy for Precision Measurement Science and Technology, Chinese Academy of Sciences, Wuhan 430071, China; University of Chinese Academy of Sciences, Beijing 100864, China*; orcid.org/0009-0006-7871-6369

Zhuang Liu − *State Key Laboratory of Magnetic Resonance and Atomic and Molecular Physics, Innovation Academy for Precision Measurement Science and Technology, Chinese Academy of Sciences, Wuhan 430071, China; University of Chinese Academy of Sciences, Beijing 100864, China*

Jie Wang − *State Key Laboratory of Magnetic Resonance and Atomic and Molecular Physics, Innovation Academy for Precision Measurement Science and Technology, Chinese*

Academy of Sciences, Wuhan 430071, China; University of Chinese Academy of Sciences, Beijing 100864, China

Martins Otikovs − *Department of Chemical and Biological Physics, Weizmann Institute of Science, Rehovot 76100, Israel*

Zhi Zhang − *State Key Laboratory of Magnetic Resonance and Atomic and Molecular Physics, Innovation Academy for Precision Measurement Science and Technology, Chinese Academy of Sciences, Wuhan 430071, China; University of Chinese Academy of Sciences, Beijing 100864, China*

Xin Cheng − *State Key Laboratory of Magnetic Resonance and Atomic and Molecular Physics, Innovation Academy for Precision Measurement Science and Technology, Chinese Academy of Sciences, Wuhan 430071, China; University of Chinese Academy of Sciences, Beijing 100864, China*

Jiazheng Wang − *Clinical & Technical Support, Philips Healthcare, Beijing 100600, China*

Lucio Frydman − *Department of Chemical and Biological Physics, Weizmann Institute of Science, Rehovot 76100, Israel;* orcid.org/0000-0001-8208-3521

Xin Zhou − *State Key Laboratory of Magnetic Resonance and Atomic and Molecular Physics, Innovation Academy for Precision Measurement Science and Technology, Chinese Academy of Sciences, Wuhan 430071, China; University of Chinese Academy of Sciences, Beijing 100864, China; Optics Valley Laboratory, Hubei 430074, China*

Maili Liu − *State Key Laboratory of Magnetic Resonance and Atomic and Molecular Physics, Innovation Academy for Precision Measurement Science and Technology, Chinese Academy of Sciences, Wuhan 430071, China; University of Chinese Academy of Sciences, Beijing 100864, China; Optics Valley Laboratory, Hubei 430074, China*

Complete contact information is available at: https://pubs.acs.org/10.1021/acs.analchem.4c01999

Author Contributions

Xinjie Liu: Methodology, Data Acquisition, Software, Writing − original draft; Qingjia Bao: Conceptualization, Methodology, Writing − review & editing, Supervision, and Project administration; Zhuang Liu, Jie Wang: Animal model, Writing − original draft; Martins Otikovs: Validation, Writing − review & editing; Zhi Zhang, Xin Chen: Validation; Lucio Frydman: Formal analysis; Xin Zhou, Maili Liu: Validation, Supervision; Chaoyang Liu: Funding acquisition, Resources, Supervision.

Notes

The authors declare no competing financial interest.

■ ACKNOWLEDGMENTS

We acknowledge Dr. Peng Sun in Clinical & Technical Support, Philips Healthcare, China. This work was supported by the National Key Research and Development Program (2023YFE0113300, 2022YFF0707000), the Strategic Priority Research Program of the Chinese Academy of Sciences (XDB0540300), the National Natural Science Foundation of China (22327901), and the Science and Technology Innovation Talent and Service Special Project of Hubei Province (2023EHA003).

■ REFERENCES

(1) Keep, R. F.; Hua, Y.; Xi, G. *Lancet. Neurology* **2012**, *11* (8), 720−31.

(2) Puy, L.; Parry-Jones, A. R.; Sandset, E. C.; Dowlatshahi, D.; Ziai, W.; Cordonnier, C. *Nat. Rev. Dis. Primers* **2023**, *9* (1), 14.

(3) Selim, M.; Hanley, D.; Broderick, J.; Goldstein, J. N.; Gregson, B. A.; Falcione, G.; Gonzales, N. R.; Gurol, E.; Kersten, J.; Lewkowicz, H.; Mendelow, A. D.; Muehlschlegel, S.; Neuman, R.; Palesch, Y.; Rosenblum, M.; Sheth, K. N.; Singh, V.; Ziai, W.; Keep, R. F.; Aronowski, J.; Genstler, C.; James, M. L.; Ratan, R.; Sansing, L.; Youd, A.; Xi, G.; Zille, M.; Anderson, C.; Awad, I.; Bastings, E.; Bednar, M.; Coon, A. L.; Gottesman, R.; Katz, B.; Khan, S.; Koenig, J.; Koroshetz, W.; Ling, S.; Loftus, C.; Lockhardt, J.; Louis, T.; Marler, J.; Moy, C.; Peña, C.; Pollack, C.; Omert, L.; Shah, M.; Shoamanesh, A.; Singer, M.; Steiner, T.; Torbey, M.; Tymianski, M.; Wakhloo, A.; Vespa, P.; Zuccarello, M.; Zheng, X. *Stroke* **2018**, *49* (5), 1308−1314.

(4) Han, X.; Ren, H.; Nandi, A.; Fan, X.; Koehler, R. C. *Sci. Rep.* **2021**, *11* (1), 10885.

(5) Zhang, X.; Zhang, Y.; Su, Q.; Liu, Y.; Li, Z.; Yong, V. W.; Xue, M. *Neurosci. Bull.* **2023**, *40*, 401−414.

(6) Loan, J. J.; Kirby, C.; Emelianova, K.; Dando, O. R.; Poon, M. T.; Pimenova, L.; Hardingham, G. E.; McColl, B. W.; Klijn, C. J.; Al-Shahi Salman, R.; Schreuder, F. H.; Samarasekera, N. *J. Neurol., Neurosurg. Psychiatry* **2022**, *93* (2), 126−132.

(7) Carteron, L.; Bouzat, P.; Oddo, M. *Front. Neurol.* **2017**, *8*, 601.

(8) Qureshi, A. I.; Ali, Z.; Suri, M. F. K.; Shuaib, A.; Baker, G.; Todd, K.; Guterman, L. R.; Hopkins, L. N. *Critical care medicine* **2003**, *31* (5), 1482−1489.

(9) Ko, S.-B.; Choi, H. A.; Parikh, G.; Helbok, R.; Schmidt, J. M.; Lee, K.; Badjatia, N.; Claassen, J.; Connolly, E. S.; Mayer, S. A. *Stroke* **2011**, *42* (11), 3087−3092.

(10) Veldeman, M.; Albanna, W.; Weiss, M.; Park, S.; Hoellig, A.; Clusmann, H.; Helbok, R.; Temel, Y.; Alexander Schubert, G. *Stroke* **2021**, *52* (11), 3624−3632.

(11) Zaro-Weber, O.; Fleischer, H.; Reiblich, L.; Schuster, A.; Moeller-Hartmann, W.; Heiss, W. D. *Annals of neurology* **2019**, *85* (6), 875−886.

(12) Vespa, P. M. *Stroke* **2009**, *40* (5), 1547−8.

(13) Reinfeld, B. I.; Madden, M. Z.; Wolf, M. M.; Chytil, A.; Bader, J. E.; Patterson, A. R.; Sugiura, A.; Cohen, A. S.; Ali, A.; Do, B. T.; Muir, A.; Lewis, C. A.; Hongo, R. A.; Young, K. L.; Brown, R. E.; Todd, V. M.; Huffstater, T.; Abraham, A.; O'Neil, R. T.; Wilson, M. H.; Xin, F.; Tantawy, M. N.; Merryman, W. D.; Johnson, R. W.; Williams, C. S.; Mason, E. F.; Mason, F. M.; Beckermann, K. E.; Vander Heiden, M. G.; Manning, H. C.; Rathmell, J. C.; Rathmell, W. K. *Nature* **2021**, *593* (7858), 282−288.

(14) Wang, Z. J.; Ohliger, M. A.; Larson, P. E.; Gordon, J. W.; Bok, R. A.; Slater, J.; Villanueva-Meyer, J. E.; Hess, C. P.; Kurhanewicz, J.; Vigneron, D. B. *Radiology* **2019**, *291* (2), 273−284.

(15) Nelson, S. J.; Kurhanewicz, J.; Vigneron, D. B.; Larson, P. E.; Harzstark, A. L.; Ferrone, M.; van Criekinge, M.; Chang, J. W.; Bok, R.; Park, I.; Reed, G.; Carvajal, L.; Small, E. J.; Munster, P.; Weinberg, V. K.; Ardenkjaer-Larsen, J. H.; Chen, A. P.; Hurd, R. E.; Odegardstuen, L. I.; Robb, F. J.; Tropp, J.; Murray, J. A. *Sci. Transl. Med.* **2013**, *5* (198), 198ra108.

(16) Guglielmetti, C.; Chou, A.; Krukowski, K.; Najac, C.; Feng, X.; Riparip, L. K.; Rosi, S.; Chaumeil, M. M. *Sci. Rep.* **2017**, *7* (1), 17525.

(17) Kaggie, J. D.; Khan, A. S.; Matys, T.; Schulte, R. F.; Locke, M. J.; Grimmer, A.; Frary, A.; Menih, I. H.; Latimer, E.; Graves, M. J.; McLean, M. A.; Gallagher, F. A. *NeuroImage* **2022**, *257*, No. 119284.

(18) De Feyter, H. M.; Behar, K. L.; Corbin, Z. A.; Fulbright, R. K.; Brown, P. B.; McIntyre, S.; Nixon, T. W.; Rothman, D. L.; de Graaf, R. A. *Sci. Adv.* **2018**, *4* (8), No. eaat7314.

(19) De Feyter, H. M.; de Graaf, R. A. *J. Magn. Reson.* **2021**, *326*, No. 106932.

(20) Pan, F.; Liu, X.; Wan, J.; Guo, Y.; Sun, P.; Zhang, X.; Wang, J.; Bao, Q.; Yang, L. *Eur. Radiol. Exp.* **2024**, *8* (1), 65.

(21) Kreis, F.; Wright, A. J.; Hesse, F.; Fala, M.; Hu, D. E.; Brindle, K. M. *Radiology* **2020**, *294* (2), 289−296.

(22) Lu, M.; Zhu, X. H.; Zhang, Y.; Mateescu, G.; Chen, W. *Journal of cerebral blood flow and metabolism: official journal of the International Society of Cerebral Blood Flow and Metabolism* **2017**, *37* (11), 3518−3530.

(23) Peters, D. C.; Markovic, S.; Bao, Q.; Preise, D.; Sasson, K.; Agemy, L.; Scherz, A.; Frydman, L. *Magn. Reson. Med.* **2021**, *86* (5), 2604−2617.
(24) MacLellan, C. L.; Silasi, G.; Auriat, A. M.; Colbourne, F. *Stroke* **2010**, *41* (10_suppl_1), S95−S98.
(25) Purvis, L. A. B.; Clarke, W. T.; Biasiolli, L.; Valkovič, L.; Robson, M. D.; Rodgers, C. T. *PloS one* **2017**, *12* (9), No. e0185356.
(26) Speck, O.; Scheffler, K.; Hennig, J. *Magn. Reson. Med.* **2002**, *48* (4), 633−9.
(27) Bogner, W.; Otazo, R.; Henning, A. *NMR Biomed.* **2021**, *34* (5), No. e4314.
(28) Montrazi, E. T.; Sasson, K.; Agemy, L.; Peters, D. C.; Brenner, O.; Scherz, A.; Frydman, L. *Sci. Rep.* **2023**, *13* (1), 19998.
(29) Li, X.; Yang, Y.; Zhang, B.; Lin, X.; Fu, X.; An, Y.; Zou, Y.; Wang, J. X.; Wang, Z.; Yu, T. *Signal Transduction Targeted Ther.* **2022**, *7* (1), 305.
(30) Inoue, Y.; Miyashita, F.; Minematsu, K.; Toyoda, K. *Journal of Stroke and Cerebrovascular Diseases* **2018**, *27* (1), 97−102.
(31) Liu, Y.; Yang, S.; Cai, E.; Lin, L.; Zeng, P.; Nie, B.; Xu, F.; Tian, Q.; Wang, J. *CNS neuroscience & therapeutics* **2020**, *26* (10), 1031−1044.
(32) Carhuapoma, J. R.; Wang, P. Y.; Beauchamp, N. J.; Keyl, P. M.; Hanley, D. F.; Barker, P. B. *Stroke* **2000**, *31* (3), 726−732.
(33) Markovic, S.; Roussel, T.; Agemy, L.; Sasson, K.; Preise, D.; Scherz, A.; Frydman, L. *NMR Biomed.* **2021**, *34* (9), No. e4569.
(34) Ruhm, L.; Avdievich, N.; Ziegs, T.; Nagel, A. M.; De Feyter, H. M.; de Graaf, R. A.; Henning, A. *NeuroImage* **2021**, *244*, No. 118639.
(35) Adamson, P. M.; Datta, K.; Watkins, R.; Recht, L. D.; Hurd, R. E.; Spielman, D. M. *Magn. Reson. Med.* **2024**, *91* (1), 39−50.

https://doi.org/10.1021/acs.analchem.4c01999
Anal. Chem. 2024, 96, 15563−15571